RSC Advances

PAPER

View Article Online
View Journal | View Issue

Cite this: *RSC Adv.*, 2022, **12**, 32156

Magnetic nanocomposites based on Zn,Al-LDH intercalated with citric and EDTA groups for the removal of U(VI) from environmental and wastewater: synergistic effect and adsorption mechanism study†

Natalia Kobylinska, * Liubov Puzyrnaya and Galina Pshinko

The efficient removal of U(VI) ions from contaminated natural waters and wastewaters of industrial processing plants by novel magnetic nanocomposites based on magnetite and Zn,Al-layered double hydroxides intercalated with citric and EDTA groups (Fe_3O_4/Zn,Al-LDH/Cit and Fe_3O_4/Zn,Al-LDH/EDTA) was shown. These adsorbents were obtained using co-precipitation and ion-exchange techniques. The infrared spectroscopy confirmed the existence of O-containing groups on the surfaces of Fe_3O_4/Zn,Al-LDH/Cit and Fe_3O_4/Zn,Al-LDH/EDTA, which could provide active sites in the interlayer of the adsorbents for the pollutants removal. The intercalation of Zn,Al-LDH with chelating EDTA-groups significantly increased the adsorption capacity toward U(VI) ions (131.22 mg g^{-1}) compared to citric moieties in a wide range of pH (3.5–9.0). The maximum adsorption capacities of U(VI) at pH 7.5 were 81.12 mg g^{-1} for Fe_3O_4/Zn,Al-LDH/EDTA and 21.6 mg g^{-1} for Fe_3O_4/Zn,Al-LDH/Cit. The higher adsorption capacity of Fe_3O_4/Zn,Al-LDH/EDTA *vs.* the citric sample might be explained by high affinity of LDH-supports and high-activity of the chelating groups in formation of the complexes in the interlayer space of the magnetic nanocomposite. The removal of U(VI) by the magnetic nanocomposites occurred due to interlayer complexation and electrostatic interactions. The cations (Na^+, K^+, Ca^{2+}), HCO_3^- and fulvic acid anions being typical for natural waters were practically not affected upon the removal of U(VI) from aqueous media. The adsorption performance of Fe_3O_4/Zn,Al-LDH/EDTA nanocomposites was evaluated in the analysis of environmental and wastewater samples with recoveries in the range of 95.8–99.9%. This superior intercalation performance of LDH-supports provides simple and low-cost adsorbents, providing a strategy for decontamination of radionuclides from wastewater.

Received 1st September 2022
Accepted 2nd November 2022

DOI: 10.1039/d2ra05503a

rsc.li/rsc-advances

1. Introduction

Over the last 50 years, radionuclides have been among the most dangerous pollutants of the environment.[1] The major sources of radionuclide ($^{235,238}U$, ^{137}Cs, ^{90}Sr, ^{60}Co, $^{152+154}Eu$ and ^{241}Am) contaminations of the last decades originated from nuclear power plants, nuclear weapon productions, nuclear fuel recycling units, and were released from nuclear cement repositories and various nuclear accidents. Radionuclides can be found in ambient air, soil, and aquatic environments after their discharge from corresponding sources especially upon accidental releases of radionuclides to the environment from Nuclear Power Plants (*i.e.* Fukushima (Japan) in 2011, Chernobyl (Ukraine) in 1986,[2] *etc.*), and leakages of liquid nuclear waste storage. Furthermore, accidents at Nuclear Power Plants and nuclear waste repositories leading to radioactive fall-outs with contamination to vegetation and soil, for example, in the Red forest in the Chernobyl Exclusion Zone district of Ukraine,[2] can cause subsequent transfer of radionuclides to the ground and river water. U(VI) is the most common radionuclide in nuclear wastes. At the same time, U(VI) is a heavy actinide with a long half-life of radioactive decay, high chemical and biological toxicity, and a non-biodegradable and carcinogenic nature which constitutes a great threat to human health.[3,4] To reduce these health risks, both World Health Organization (WHO) and the United States Environmental Protection Agency (USEPA) set a guideline limit for total U(VI) content in drinking water at 30 ppb.[5] Uranium concentrations in the groundwater of the contaminated zone were much higher than the safety limit.[2] Thus, monitoring and subsequent removal of U(VI) from

Dumansky Institute of Colloid and Water Chemistry, National Academy of Sciences of Ukraine, 42 Akad. Vernadsky Blvd., Kyiv, 03142, Ukraine. E-mail: kobilinskaya@univ.kiev.ua

† Electronic supplementary information (ESI) available: XRD patterns, scanning electron microscopy images, effect of pH, kinetic and isotherm fitting plots for the adsorption of uranium(VI) onto obtained samples, equilibrium constants of U(VI) in solution. See DOI: https://doi.org/10.1039/d2ra05503a

contaminated water including U(VI)-containing nuclear waste is one of the major environmental remediation problems of today.[4] Numerous studies have shown[6] that U(VI) is present in environmental water and wastewater mainly in the soluble anionic carbonate forms such as $UO_2(CO_3)_2^{2-}$ and $UO_2(CO_3)_3^{4-}$ which are not sufficiently eliminated by mineral suspensions and clay components of soils.

Numerous methods have been proposed to remove U(VI) from waste and contaminated environmental water[7] such as solvent extraction,[8] distillation,[9] coagulation,[10] reverse osmosis,[11] precipitation,[12] adsorption/ion exchange,[13] membrane filtration and biological technologies.[14] Each of these methods has its advantages and disadvantages. For example, coagulation using ferric sulfate, ferrous sulfate, or aluminum is an efficient method but the efficiency greatly depends on the pH value of water. Removal efficiencies of more than 80% can be achieved only at higher pH (near 10) values. This means that at pH values typical of natural waters, coagulation and lime softening is not effective. The long precipitation time that is required makes the process impractical with large volumes of wastewater. The important way for the removal of U(VI) is the reductive precipitation in anaerobic conditions, in which U(VI) is reduced to U(IV), which is insoluble and thus its can be removed from water by precipitation. Usually, the zero-valent iron (Fe^0)[15] and denitrifying bacteria[16] were used as reducing agents. In water and especially water containing dissolved oxygen, Fe^0 is quickly oxidized to Fe(II)/Fe(III), which leads to a rapid loss of the reducing capacity.[17] Other common dissolved solutes such as bicarbonate/carbonate and oxygen from water medium also cause corrosion of Fe^0.[18] U(VI) was removed by Fe^0 systems down to concentrations <10 μg L^{-1} (recovery >98%), and partial chemical reduction of U(VI) to U(IV) concurrent with Fe oxidation was confirmed.[19] In contrast under these conditions, Fe_3O_4 sample achieved U(VI) removal >20% from the carbonate-rich environmental water. Both nanomaterials are ineffective at timescales >1 week contact because of uranium re-release into water. This behavior is attributed to the high stability of uranium complexes in the presence of carbonate or other ligands present in the natural water. Consequently, further research is required to develop materials that exhibit extended retention of inorganic contaminants including uranium from chemically complex environmental waters. Reverse osmosis is very effective (removal ≥ 99%),[11] however, this method is pretty expensive and causes big changes in water composition, which makes these devices not applicable for drinking water treatment.[11] Among published approaches to removal of U(VI) from aqueous solutions, the adsorption technique is considered as the most popular pathway due to economy and efficiency in purification of U(VI)-contaminated wastes. Previously, U(VI) ion removal by adsorption was studied on several adsorbents such as activated carbon,[20,21] hydrogels,[22] ion-imprinted polymers,[23] and various composite materials,[24–26] *etc.*

During recent years, a lot of scientific studies have been focused on the removal of uranium(VI) from contaminated water using layered double hydroxides (LDH) and corresponding composites.[25–28] This tremendous attention may be attributed to a good combination of physicochemical properties such as high stability, excellent anion exchange capacity, and relative easiness of modification of the surface by selective functional groups to increase surface concentration of active adsorptive centers towards U(VI) ions. For example, Ma S. *et al.*[29] applied Mg,Al-LDH modified by polysulfide to remove uranium efficiently from environmental water and specifically seawater. However, the authors described sorption of UO_2^{2+} species without taking into account uranium–carbonate complexes which prevail in water solution. It was reported[30] that phytic acid modified Zn–Al–Ti metal oxide was used to remove U(VI) from wastewater. Phosphate functionalized LDH were synthesized for efficient U(VI) uptake from polluted solutions,[31] but in this case it is necessary to take precautions to avoid the eutrophication of water bodies. Linghu W. highlighted the application of Mg,Al-LDH/GO-based composites for removal of U(VI) in environmental cleanup.[26] The magnetic separation technique was shown to be a promising method for solid–liquid phase separation of sorbent from water matrices with an external magnetic field particularly for the removal of radionuclides including U(VI) ions.[32] Most of these adsorbents were magnetite-based, while other magnetic materials such as Fe^0 (ref. 17 and 19) could be also applicable. The sorption of U(VI) on pristine magnetite nanoparticles with relatively small adsorption capacity at pH 7.0 was demonstrated by Das *et al.*[33] Compared to the pristine magnetite, the Mn-doped ferrite nanomaterials exhibited generally superior adsorption performance towards U(VI) uptake in the pH range from 4 to 7.[34] In order to impart improved adsorption abilities towards U(VI) to magnetite, it is modified *via* introduction of specific functional groups or its combination in composite materials with different inorganic or organic compounds.[33,35,36] The S-doped magnetite hollow spheres used for the removal of UO_2^{2+} with a large adsorption capacity up to 450.0 mg U(VI) per g was reported.[37]

Recently, high potential of chelating groups intercalated in the LDH-based materials was used for removal of U(VI) ions from an aqueous solution (removal > 70%).[38,39] Since the interlayer of functional groups is easily formed from coordination compounds with various U(VI) forms, it makes LDH useful for the adsorption applications. Previously, many studies were published about adsorption of various metal ions including U(VI) ions by materials containing functional ethylenediaminetetraacetic (EDTA) groups.[40,41] On the other hand, synthesis of the EDTA-intercalated LDH-based magnetic nanocomposites with high adsorption capacity and selectivity towards U(VI) ions has not been performed until today.

This work is devoted to preparation of EDTA and citric acids intercalated Zn,Al-layered double hydroxide magnetic nanocomposites (Fe_3O_4/Zn,Al-LDH/EDTA and Fe_3O_4/Zn,Al-LDH/Cit) *via* a facile and simple step-by-step co-precipitation method and ion-exchange techniques. These adsorbents were applied for effective, high selective removal of U(VI) from environmental and wastewaters. Various characterization techniques were used to investigate the interaction mechanism of the anionic radionuclide forms with Fe_3O_4/Zn,Al-LDH/EDTA and Fe_3O_4/Zn,Al-LDH/Cit. The uptake performance and selectivity of the obtained adsorbents towards U(VI) ions were minutely studied under

influence of various experimental factors (pH and HCO_3^-/CO_3^{2-} effects, contact time, adsorption capacity, coexisting ions, *etc.*). Finally, a possible use of the synthesized magnetic nanocomposites as adsorbents for the removal of U(VI) from environmental and industrial wastewaters was demonstrated.

2. Experimental

2.1. Preparation of adsorbents

2.1.1 Synthesis of Fe_3O_4. Magnetic nanoparticles were synthesized by chemical co-precipitation of ferric and ferrous sulfate salts using NaOH. Briefly, to the 250 mL of distillated water in Erlenmeyer flask, 13.9 g (0.05 mol) of $FeSO_4 \cdot 7H_2O$ and 28.1 g (0.05 mol) of $Fe_2(SO_4)_3 \cdot 9H_2O$ salts were added with molar ratio $n(Fe^{3+}) : n(Fe^{2+}) = 2:1$. After adding 400 mL of CO_2-free distilled water the obtained mixture was mechanically stirred, and, then, a 30 wt% aqueous solution of NaOH was added with constant stirring to pH 10.0 ± 0.5. The mixture was heated up to 70 °C with constant stirring for further 2 hours under N_2 atmosphere. The precipitate was washed with deionized water several times until the negative reaction of sulfate-ions and stored in ethanol solution (400 mL) without drying.

2.1.2 Synthesis of LDH-based samples. All LDH-based samples were prepared by a co-precipitation method according to a modified procedure.[38] For this purpose, 0.67 M $ZnCl_2$ and 0.33 M $AlCl_3$ was dissolved in deionized water to prepare a mixed solution in the flask (pH = 2). The mixture of NaOH (2 mol) and Na_2CO_3 (1 mol) was added using a peristaltic pump with rate of 5 cm^3 min^{-1}. The solution pH was adjusted to 9.0. After addition of the solution, the reaction mixture was stirred during 3 days at 60–70 °C with constant pH (by adding NaOH or HCl). Then, the precipitate was separated by centrifugation (4500 rpm) during 30 min and washed with distilled water to a negative reaction with $AgNO_3$ solution. The obtained sample was dried at 60 °C overnight. The obtained sample is denoted as Zn,Al-LDH/CO_3.

The intercalation compounds (Zn,Al-LDH/Cit and Zn,Al-LDH/EDTA) were prepared from Zn,Al-LDH/CO_3 by anion-exchange reaction. Typically, Zn,Al-LDH/CO_3 (20 g) solid was added to 400 mL of distillated water at temperature 50 °C to obtain a suspension. To the resultant suspension at constant stirring was added solution of 44.1 g (0.21 mol) of citric acid (or 0.015 M Na_2H_2EDTA) by dropwise (at 5 mL min^{-1}) under nitrogen atmosphere. The products were washed with distilled water, followed by being dried for 24 h at 50 °C.

2.1.3 Synthesis of magnetic nanocomposites. Before the magnetic nanocomposite synthesis both suspension of as-prepared Fe_3O_4 (5.6 g) in 200 mL distilled water (CO_2-free) and a suspension of Zn,Al-LDH/Cit (or Zn,Al-LDH/EDTA) (24.3 g) in 400 mL of distilled water were ultrasonically treated during 1 hour at room temperature. Then, these suspensions of the Zn,Al-LDH/Cit (or Zn,Al-LDH/EDTA) and the pristine magnetite were mixed with continuously mechanical agitation in water bath (10 min) at 70 °C, and sonicated for 30 min. The target solids were formed during 24 hours. Then, the obtained solids were magnetically separated from reaction mixture. These nanocomposites are washed two times with distilled water and dried at 60 °C for 18 h.

2.2. Characterization of the adsorbents

For the quantification of the main elements present in the samples, the solids (0.1000 g) were dissolved in 15–20 mL of diluted HCl (1 : 1) and CO_2-free distilled water (total 100 mL), and analyzed in duplicate with the atomic absorption spectroscopy (C-115-M1 spectrometer) at 213.9 nm (Zn), 309.3 nm (Al) and 248.3 nm (Fe). The content of organic functional motives was determined using total organic carbon analysis.[42] The obtained data were used in the compounds' formulations.

Temperature and field dependent magnetic measurements of obtained samples were measured with EV9 vibrating sample magnetometer under the high sensitivity reciprocal space option. The size and morphology of the nanoparticles were examined using transmission electron microscopy (TEM), on JEM-2100F (JEOL, Japan) operated at 200 kV and equipped with an ultra-high resolution pole-piece. The samples were sprayed on a carbon coated copper grid, and then exposed to air-drying. The surface topography of the nanoparticles was studied using scanning electron microscopy (SEM), JSM-6100 (JEOL, Japan). To increase the optical contrast, the samples were covered with gold on superfine spraying instrument JFC-1600 Auto Fine Coater (JEOL, Japan). The chemical composition of the nanoparticles was determined by energy dispersive X-ray analysis (EDX) on Microanalysis INCA Energy 200 equipped with an Oxford PentaFET ultrathin window detector attached to a scanning electron microscope. The powder X-ray diffraction (XRD) data were collected using PANalytical X'Pert Pro diffractometer with CuKα radiation (λ = 1.5405 Å). Measurements over the range $5° \leq 2\theta \leq 120°$ with a step size of 0.040° were performed at room temperature. The thermal analysis measurements (TG/DTG and DTA curves) were obtained in Mettler Toledo TGA/SDTA851 equipment, using platinum crucibles, flow of nitrogen, and heating rate of 10 min^{-1}. The total amount of intercalated organic groups (C_L, mmol g^{-1}) for LDH-based samples was determined from TG curves. Assuming that the initial samples and intercalated samples after 1000 °C treatment have the same extent of surface hydroxylation, the following formula was used for the calculations

$$C_L = \Delta m_{200-500} m_{initial} / 100M \quad (1)$$

where $\Delta m_{200-500}$ is the weight loss of the sample at the temperatures between 200 and 500 °C, %; $m_{initial}$ is the weight of the initial sample dried at 100 °C, mg; M is the molecular mass of organic residues.

The N_2 adsorption/desorption isotherms at 77 K were performed using a KELVIN 1042 BET-Sorptometer (Costech International). Prior to measurements, the samples (50 mg) were outgassed at 110 °C for 4 h under a vacuum above 10^2 Pa. The porosity of the samples was analysed by applying the nonlocal density functional theory (NLDFT).[43]

The Fourier transform infrared spectra (FTIR) of the samples were recorded in the 4000–400 cm^{-1} range, on Spectrum BX FTIR spectrometer (PerkinElmer, USA). The sample was

thoroughly ground with KBr (1 : 10), after that they were tableted under load 1.7 t cm^{-2}.

2.3. Batch adsorption experiments

The influence of pH on U(VI) removal was tested for all obtained adsorbents at room temperature. For the preparation of stock solutions was used $UO_2SO_4 \cdot 3H_2O$ (≥98%).

Typically, 100 mg of solids were mixed with 50 mL of the solution containing 0.1 mmol L^{-1} of U(VI) in the centrifuge tube; the suspension pH in the range of 2.0–10.0 was adjusted by adding HNO_3 (0.1 M) or NaOH (0.1 M). The pH (±0.005) value of the solution before and after adsorption process was measured using an I-160 M ionometer. The mixtures were agitated by orbital shaker (AVU-6S) during 1 h. After equilibrium, the solid phase was magnetically separated from liquid phase. The concentration of U(VI) in supernatant was measured by spectrophotometry with Arsenazo III at $\lambda = 656$ nm in 5–7 M HNO_3. The limit of determination of U(VI) by this method is 5 μg. All adsorption experiments were performed in triple parallel tests.

The adsorption kinetic experiments was carried out by changing the contact time from 0 to 120 min between the 0.10 g of solid and 50 mL of 0.1 mmol L^{-1} U(VI) solution at $pH_{initial} = 5.0 \pm 0.1$. The aliquots were collected at the times 0, 5, 15, 30, 60, 90 and 120 min, respectively. The removal of U(VI) ions (R, %) and adsorption capacity (q_e) were determined as follows:

$$R(\%) = C_0 - C_e/C_0 \times 100\% \quad (2)$$

$$q_e\ (\text{mg g}^{-1}) = (C_0 - C_e)VM/g \text{ or } q_e\ (\text{mmol g}^{-1}) = (C_0 - C_e)V/g \quad (3)$$

where C_0 and C_e are the initial and equilibrium concentration of U(VI) in solution, respectively, mmol L^{-1}; V is the volume of the solution, mL; M is molecular mass of analyte, g mol^{-1}; g is the adsorbent weight, mg.

Adsorption isotherms were carried out by the batch equilibration technique at room temperature. The solids (0.1 g) were dispersed in 50 mL of U(VI) solution with concentration varying from 0.15 to 0.90 mmol L^{-1} U(VI) solutions were prepared in an appropriate range of concentrations to obtain a final volume of 50 mL after the addition of the adsorbent and the pH was fixed at 7.5. Then, suspension is shacked during 24 h. After that the adsorbent was magnetically separated and the remaining concentration of the metals in solution was determined by spectrophotometry. The q_e value was determined from the eqn (2).

2.3.1 The point of zero charge (pH_{pzc}) determination. To determine the pH_{pzc} value of the obtained samples was used the pH drift method.[44] Briefly, 0.025 g of solid was added into the 0.1 mmol L^{-1} U(VI) solution (25 mL) with different $pH_{initial}$. The $pH_{initial}$ of solution was in the range of 2 to 10 with an increment of ~0.5 pH units. The suspension was continuously stirred during 24 h for reach to equilibrium. Then, the pH_{final} values were measured.

2.4. Competitive adsorption of metal ions

2.4.1 U(VI)-containing model solutions. To study the effect of macrocomponents of environmental and wastewaters on the sorption of U(VI) were used inorganic salts (NaCl, KCl, $CaCl_2 \cdot 6H_2O$ and $NaHCO_3$) analytical grade with concentration from 20 to 200 mg L^{-1}. The effect of natural organic components was studied using fulvic acids (FA) isolated from sapropels of the lake. The total amount of FA was 12.0 mg eq g^{-1}.

2.5. Genuine water assay

To demonstrate the applicability and reliability of the synthesized adsorbents for water treatment were used river water and wastewater. The real wastewater samples were collected from uranium processing State Enterprise "Eastern Mining and Processing Plant" (Zhovti Vody city, Dnipro region, Ukraine).

Briefly, main parameters of the tested water samples:

• Environmental water: pH ≈ 7, alkalinity 8.5 mg-eq L^{-1}, hardness 28 mg-eq L^{-1}, NO_3^- 470 mg L^{-1}, SO_4^{2-} 269 mg L^{-1}, Cl^- 280 mg L^{-1}, Na^+ 90 mg L^{-1}, total salt content ~2820 mg L^{-1}, chemical oxygen demand (COD) 1.6 mg O per L;

• Wastewater: pH ≈ 8, HOC_3^- 235 mg L^{-1}, CO_3^{2-} 29 mg L^{-1}, SO_4^{2-} 470 mg L^{-1}, Cl^- 280 mg L^{-1}, Ca^{2+} 170 mg L^{-1}, Na^+ 241 mg L^{-1}, Mg^{2+} 54 mg L^{-1}, U(VI) 0.85 mg L^{-1}, total salt content ~1500 mg L^{-1}, COD 59.0 mg O per L.

The real water samples were analyzed after spiking with 0.1 mmol L^{-1} of U(VI) ions for reliably determination of U(VI) ions in solution by spectrophotometry method.

3. Results and discussion

3.1. Preparation and characterisation of nanocomposites

In this work, the synthesis of Fe_3O_4/Zn,Al-LDH/Cit and Fe_3O_4/Zn,Al-LDH/EDTA nanocomposites was performed in a three-step process: (1) preparation of magnetite nanoparticles; (2) fabrication of Zn,Al-LDH/CO_3 and its modification with citric (or EDTA) groups through co-precipitation and ion-exchange techniques; (3) formation of magnetic nanocomposite based on pristine Fe_3O_4 and Zn,Al-LDH/Cit (or Zn,Al-LDH/EDTA) samples. The whole routes were represented in Scheme 1.

The size, shape and chemical composition of the magnetic nanoparticles strongly depend on the preparation conditions, which affect the efficiency of the uptake U(VI). Therefore, all synthetic steps were controlled using instrumentation techniques.

According to SEM (Fig. S1†) and TEM data (Fig. 1), significant differences exist in morphology target magnetic nanocomposites and starting materials. The TEM image (Fig. 1a) show that the pure Fe_3O_4 nanoparticles present near-spherical form with rough surface and approximate diameter of ~6–8 nm. Whereas Fig. 1b show that Zn,Al-LDH/Cit possess spherical and rod-like shapes, and the average diameter varied in the range of 24.7–82.4 nm. The Zn,Al-LDH/EDTA sample exhibit sieve-like structure. The TEM image of Fe_3O_4/Zn,Al-LDH/Cit and Fe_3O_4/Zn,Al-LDH/EDTA (Fig. 1c–e) exhibits the multiple layers of LDH around Fe_3O_4. The dark well-dispersed magnetite nanoparticles were interred consistently in LDH particles of the light grey color.

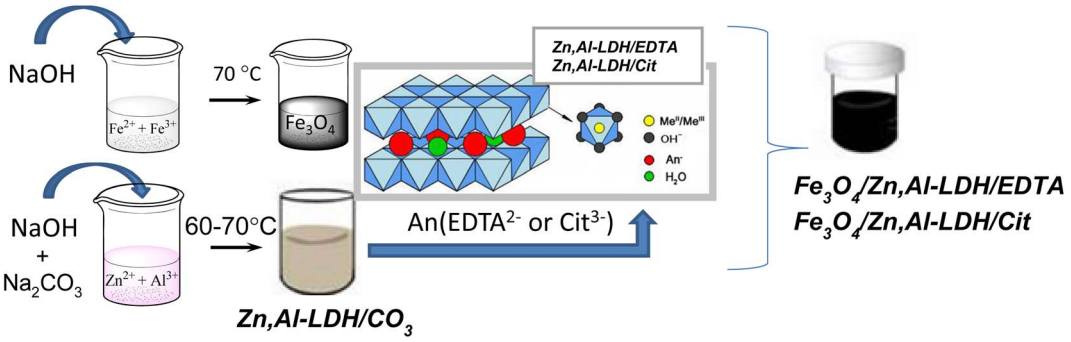

Scheme 1 Schematic illustration of preparation of Fe_3O_4/Zn,Al-LDH/Cit and Fe_3O_4/Zn,Al-LDH/EDTA nanocomposites.

SEM images of Zn,Al-LDH/Cit and Zn,Al-LDH/EDTA reveal the lamellas shapes (Fig. S1b and d†). The flakes are about 1–2 μm in size and have sub-μm thickness.

Powder XRD data was used to the phase identification of starting samples and resulted magnetic nanocomposites (Fig. 2). The XRD patterns of Fe_3O_4 show the diffraction peaks at 2θ = 30.1°, 35.5°, 43.1°, 53.4°, 57.0°, 62.5°, and 75.0° which related to the corresponding (220), (311), (400), (422), (511), (440) and (533) Bragg reflections, respectively. This data indicates that the resulted nanoparticles were magnetite (JCPDS Card No. 19-0629) with a face-centered cubic spinel crystalline structure. The average crystallite sizes calculated using Scherrer equation[45] for the (311) reflection of magnetite are 22.5 nm, 13.9 nm and 15.4 nm for Fe_3O_4, Fe_3O_4/Zn,Al-LDH/Cit and Fe_3O_4/Zn,Al-LDH/EDTA, respectively.

A dominating feature powder XRD patterns of most layered compounds is the series of reflections corresponding to the basal plane d spacing ("harmonic" peaks). Furthermore, according to Bragg's law,[46] the Zn,Al-LDH/CO_3 powder XRD pattern displays first-, second, third-, and fourth-order peaks at 7.59 Å, 3.78 Å, 2.59 Å, and 2.29 Å, respectively (Fig. S2†). The intercalated samples and its starting samples (Zn,Al-LDH/Cit and Zn,Al-LDH/EDTA) appear basal reflections, indicating the presence of the layers sequences. The XRD patterns of Zn,Al-LDH/Cit displays first-, second-, and third-order peaks at 2θ = 7.21, 14.47, and 21.8° corresponds to the basal reflections (003), (006), and (009), respectively, matching of LDH compound,[47] with several additional reflection peaks from ZnO impurity (JCPDS Card No. 36-1451) were found as result of the adverse reaction:

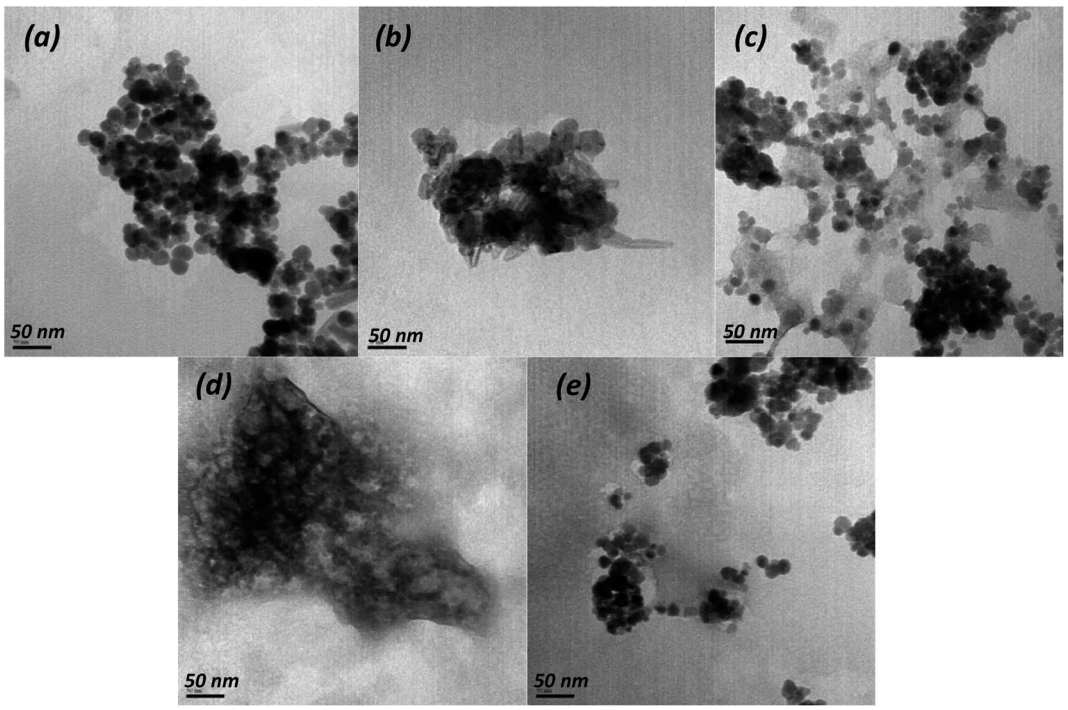

Fig. 1 TEM images of pristine Fe_3O_4 (a), Zn,Al-LDH/Cit (b), Fe_3O_4/Zn,Al-LDH/Cit (c), Zn,Al-LDH/EDTA (d) and Fe_3O_4/Zn,Al-LDH/EDTA (e) samples.

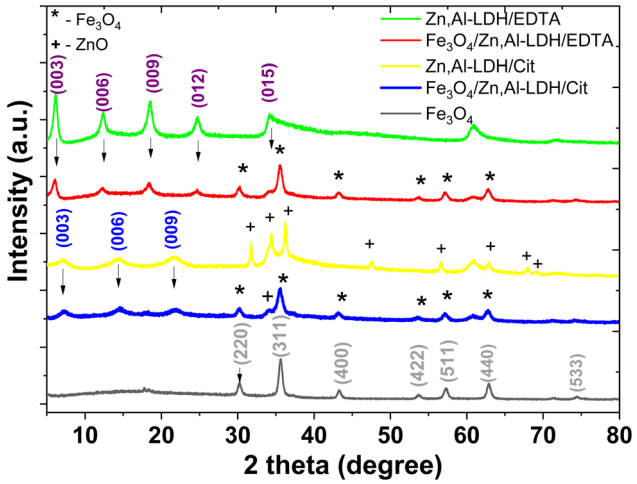

Fig. 2 Powder XRD patterns of the synthesized solids.

$$2ZnCl_2 + 2C_3H_5O(COOH)_3 + 9O_2 \rightarrow 2ZnO + 12CO_2 + 6H_2O + 4HCl$$

The basal spacing (d_{003}) for Zn,Al-LDH/Cit is 12.25 Å. This is indicative of the significantly (~40%) increase basal spacing of Zn,Al-LDH/CO_3 after intercalation. The XRD pattern of Zn,Al-LDH/EDTA display first-, second-, third- and fourth-order reflection peaks. As expected, the XRD patterns of Fe_3O_4/Zn,Al-LDH/EDTA and Fe_3O_4/Zn,Al-LDH/Cit samples containing the peaks corresponding basal reflections LDH and Fe_3O_4, proves that both phases are present in the structure of magnetic layered nanocomposites (Fig. 2). Because of the intercalation of citric or EDTA groups in LDH compound, a shift (00*L*) of the basal reflections occurs towards lower angles with a corresponding increase in *d*-spacing. Comparison of the XRD patterns revealed that the XRD peaks for magnetic composites are weakened and broadened compared to those for Zn,Al-LDH/Cit and Zn,Al-LDH/EDTA samples. For Fe_3O_4/Zn,Al-LDH/Cit, incorporation of the magnetite in Zn,Al-LDH/Cit basal spacing is almost constant. Thus, compared to the initial sample d_{003} of the intercalated Fe_3O_4/Zn,Al-LDH/EDTA samples reached 14.57 Å, respectively. These results suggest that EDTA groups was intercalated into the interlayer space of the Fe_3O_4/Zn,Al-LDH/EDTA, which was attributed to its high specific surface area. Applying Debye–Scherrer equation for the most intense diffraction peaks, crystallite sizes of bare magnetite and derivated magnetic nanocomposites were estimated (Table 1).

Generally, the average particle size estimated by TEM method have commensurate with crystallite size from XRD data.

To characterize the surface properties of the magnetic nanocomposites studied N_2 adsorption/desorption isotherm measurements were carried out for all synthesized materials and the experimental data are shown in Fig. 3. To ensure proper removal of physically adsorbed water before the adsorption measurements were taken, the layered structure were outgassed for 2 h at 120 °C under vacuum (10^{-4} Torr).

N_2 isotherms adsorption/desorption of Fe_3O_4 sample exhibit the type I without hysteresis loops according to the IUPAC classification,[48] which is typical for microporous material (Fig. 3a). The rest of the isotherms were type IV that possessed a characteristic H_3-type hysteresis loop (p/p_0 > 0.4), which indicated that the materials belongs to sheet-type materials with mesoporous structure.[48] The specific surface area of obtained samples decrease in the following order: Zn,Al-LDH/EDTA (127.69 m^2 g^{-1}) > Fe_3O_4/Zn,Al-LDH/EDTA (116.08 m^2 g^{-1}) > Zn,Al-LDH/Cit (91.60 m^2 g^{-1}) > Fe_3O_4/Zn,Al-LDH/Cit (52.18 m^2 g^{-1}) > Fe_3O_4 (11.70 m^2 g^{-1}). The pores per size distribution were estimated by using the NLDFT model giving the average pore size values (Fig. 3b). Concurrently, the respective average pore diameters and pore volumes were 1.59 nm and 0.52 cm^3 g^{-1} for Zn,Al-LDH/EDTA, 1.22 nm and 0.18 cm^3 g^{-1} for Fe_3O_4/Zn,Al-LDH/EDTA, 0.8 nm and 0.14 cm^3 g^{-1} for Zn,Al-LDH/Cit, 0.61 nm and 0.10 cm^3 g^{-1} for Fe_3O_4/Zn,Al-LDH/Cit, and 0.29 nm and 0.09 cm^3 g^{-1} for Fe_3O_4/Zn,Al-LDH/Cit, respectively. Clearly, the intercalation of samples by EDTA-groups leads to a larger specific surface area and pore volume than the intercalation by citric acid. Although the obtained magnetic nanocomposites induced smaller specific surface area than pure Zn,Al-LDH/EDTA and Zn,Al-LDH/Cit first ones still enables as an effective adsorbents.

Table 1 The main physical characteristics of obtained samples

Parameters		Fe_3O_4	Zn,Al-LDH/CO_3	Zn,Al-LDH/Cit	Fe_3O_4/Zn,Al-LDH/Cit	Zn,Al-LDH/EDTA	Fe_3O_4/Zn,Al-LDH/EDTA
2θ	(003)	—	13.4	7.2	7.15	6.1	6.2
	(006)	—	27.2	14.5	14.4	12.3	12.4
	(009)	—	40.1	21.8	21.5	19.4	19.5
Crystallite size, nm		7.1	—	—	12.1	—	11.1
Particle size, nm		6–8	—	24.7–82.4	14.5–22.1	12.7–14.4	12.8–25.6
S, m^2 g^{-1}		11.70		91.60	52.18	127.69	116.08
D_{pore}, nm		0.3	—	0.8	0.61	1.59	1.22
M_s, emu g^{-1}		66.16	—	—	20.05	—	18.06
H_C, Oe		2.2	—	—	1.5	—	1.4
C_L, mmol g^{-1}		—	—	0.040	0.028	0.029	0.015
pH_{pzc}		—	—	8.53	6.91	6.93	7.34

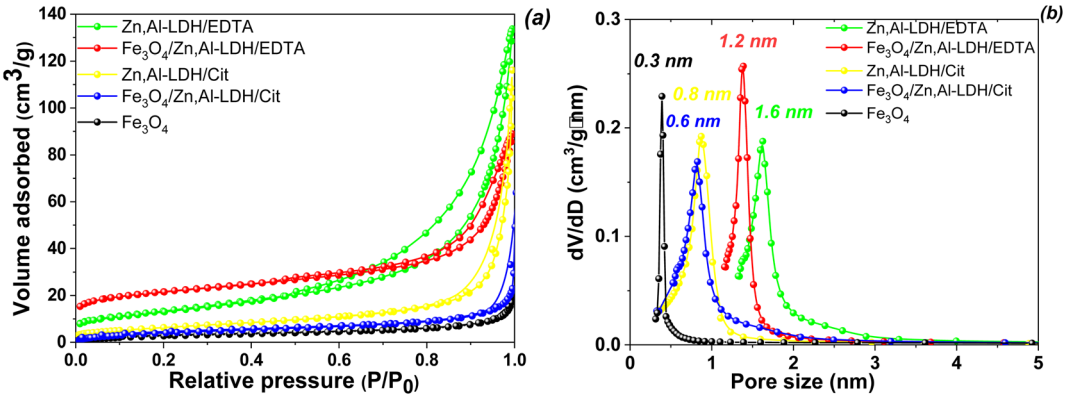

Fig. 3 N_2 adsorption/desorption isotherms (a) and pore distribution (b) of obtained samples.

The magnetic behaviour of the magnetite and derived magnetic nanocomposites were studied at room temperature (Fig. 4).

Magnetization curves for pristine Fe_3O_4 and nanocomposites passed near the zero point of magnetization field (Fig. 4). The saturation magnetization (M_s) values of Fe_3O_4/Zn,Al-LDH/EDTA and Fe_3O_4/Zn,Al-LDH/Cit samples are 20.05 and 18.06 emu g^{-1}, respectively, which are lower than that of pristine magnetite nanoparticles (M_s = 66.16 emu g^{-1}). The lower values saturation magnetization of both magnetic nanocomposites could be explained by the presence of diamagnetic Zn,Al-LDH in this samples. The magnetic hysteresis loops for these samples pointed to superparamagnetic behaviour in which remanent magnetization and coercivity (H_C) parameters were close to zero (Table 1).

Finally, the saturation magnetisation value of magnetic nanocomposites enables to separate the adsorbents from liquids using an external magnet during magnetic solid phase extraction.

The zero-field cooled (ZFC) and field-cooled (FC) magnetization curves of obtained magnetic samples were measured at low magnetic field (80 Oe) in the temperature range of 5–380 K, on the pristine magnetic nanoparticles (Fig. 5a and b) as well as on the derivated magnetic nanocomposite (Fig. 5c and d).

The main differences between the magnitude and temperature variations of the coercivities of the studied samples are reflected in the extent of the irreversibility appeared by the difference between the FC and ZFC curves (Fig. 5). The ZFC and FC curves of are typical for systems of magnetic monodomain magnetic nanoparticles presenting superparamagnetic behavior above a temperature which is called the blocking temperature. In the present case, the two curves show a divergence point very close to the maximum of the ZFC curve, suggesting both very weak interparticle magnetic interactions as well as a very narrow size distribution of the nanoparticles in the samples. On the other hand, the blocking temperature as estimated from the maximum of the ZFC curve is lower in the case of pristine magnetite nanoparticles (315 K) as compared to the case of the obtained nanocomposite (about 350 K). Keeping in mind that the blocking temperature, defined as a parameter which is dependent on the time window of the measuring method, is proportional to the anisotropy energy of the nanoparticle. It results directly that the anisotropy energy of Fe_3O_4/Zn,Al-LDH/EDTA magnetic nanocomposite is some 10% larger than of pristine magnetite in the nanosized level.

The formation of Fe_3O_4/Zn,Al-LDH/EDTA and Fe_3O_4/Zn,Al-LDH/Cit were studied by FTIR technique (Fig. 6). The broad absorption band observed around 3400 cm^{-1} corresponds to the O–H stretching valence vibration of hydroxyl groups and/or interlayer-bonded water molecules. The absorption band observed around 570 cm^{-1} belongs to Fe–O stretching and torsional mode of Fe_3O_4. Other bands observed in the low-frequency region of the spectrum (<700 cm^{-1}) are interpreted as the lattice vibration modes, such as the M–O (M = Zn, Al) vibration stretching of LDH. The peaks at 2850, 2930 and 1411 cm^{-1} are attributed to CH-stretching vibrations of intercalated functional groups. The FTIR spectra of LDH-based samples showing peaks at 1100 cm^{-1}, 1393 cm^{-1}, 1593 cm^{-1} indicating the presence of symmetrical and asymmetrical stretching vibrations of the carboxylic motives of intercalated functional groups. For Zn,Al-LDH/EDTA and Fe_3O_4/Zn,Al-LDH/

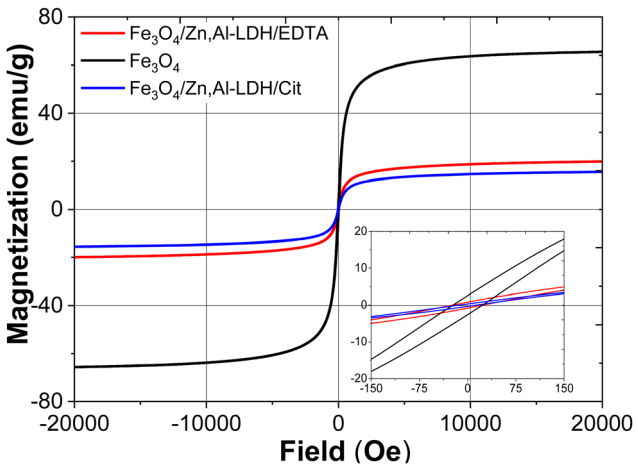

Fig. 4 Wide and narrow (insert) magnetic hysteresis loops of bare Fe_3O_4, Fe_3O_4/Zn,Al-LDH/EDTA and Fe_3O_4/Zn,Al-LDH/Cit samples at room temperature.

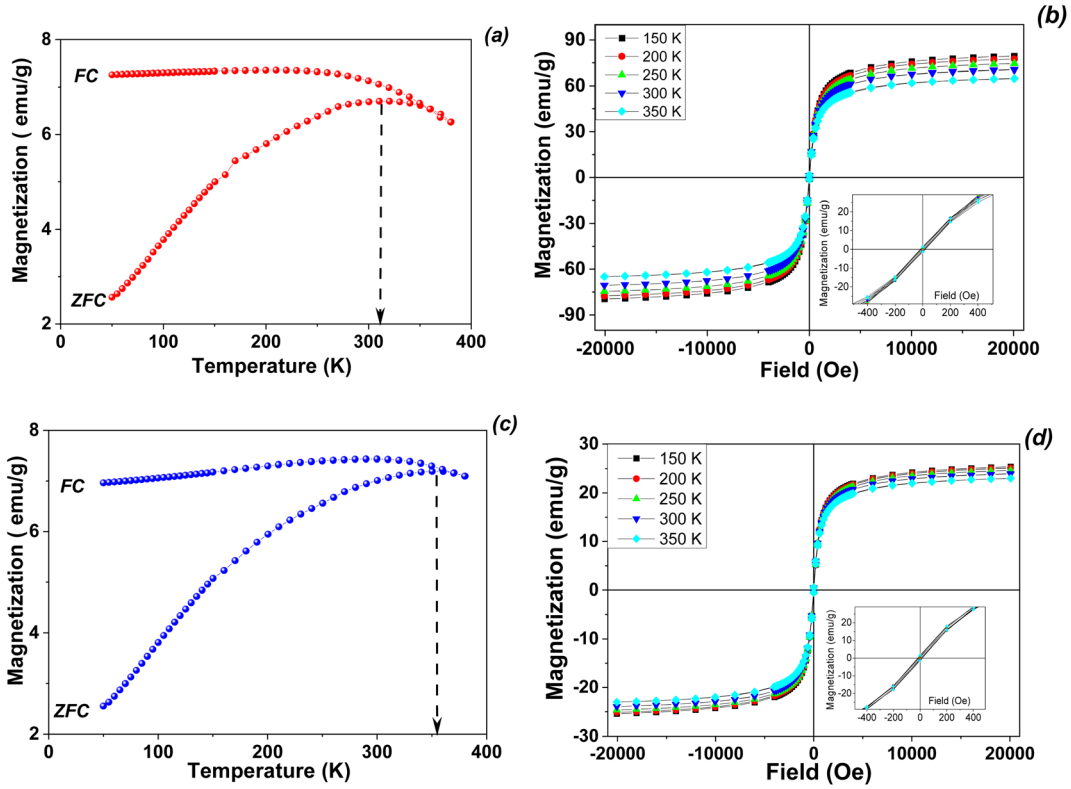

Fig. 5 ZFC/FC magnetization curves (a and c) and temperature dependent hysteresis loops (b and d) for pristine magnetite (a and b) and Fe_3O_4/Zn,Al-LDH/EDTA nanocomposite (c and d).

EDTA samples (Fig. 6b), the two low intensity bands of ν(C–N) are located at 1030–1270 cm^{-1}. Also, the peak at 1175 cm^{-1} may be assigned to ν(C–O) vibration in C–O–N motives of EDTA-groups. In the Fe_3O_4/Zn,Al-LDH/Cit nanocomposite, the symmetric C=O vibration peak at 1593 cm^{-1} shows a slight shift to higher frequency regions, when compared with those of the Zn,Al-LDH/Cit sample around 1581 cm^{-1} (Fig. 6a). This effect indicates that there is interaction between the intercalated citric groups and magnetite. Comparing the spectra of Fe_3O_4/Zn,Al-LDH/EDTA and Zn,Al-LDH/EDTA sample, the C=O stretching region did shift toward higher wavenumbers, indicating that intercalated functional groups are more free in the interfacial layer of Fe_3O_4/Zn,Al-LDH/EDTA. All these bands indicated the formation of chelating groups on the obtained solids and it could be concluded that the synthesis procedure had successfully. The introduction of magnetite into LDH structure and the change of CO_3^{2-}-groups to chelating motives are beneficial to U(VI) adsorption from aqueous solutions.

To evaluate the thermal stability of adsorbents was used thermogravimetric analysis data. In the TG/DTG and DTA, curves of studied samples (Fig. 7), there are three main steps of mass loss, which occur as endothermic processes. The water

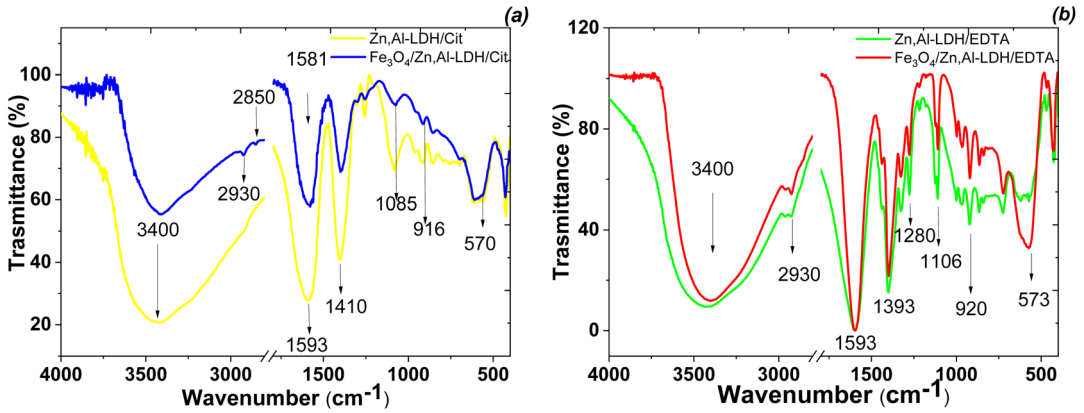

Fig. 6 FTIR spectra of synthesized magnetic nanocomposites (Fe_3O_4/Zn,Al-LDH/Cit (a) and Fe_3O_4/Zn,Al-LDH/EDTA (b)) and its intermediates.

loss up to around 60 and 120 °C, due to different types physically bonded water molecules, attributed to Fe_3O_4 and LDH parts of the samples, respectively. The mass lost occurred at 120 °C was most likely due to the loss of interlayer water of LDH. The second mass loss of LDH-based samples was the largest. It occurred at 250–400 °C and accounted until 30% of total mass loss. Asymmetry of the corresponding peaks in the DTG curve indicates that several different processes are occurring simultaneously. Indeed the comparison of TG/DTG curves between the starting LDH and their corresponding intercalated magnetic composites demonstrate that the citric and EDTA groups decomposition observe around 280 °C shifted to 330 °C and up to 400 °C. Thus, the second major weight loss occurring in the range of 250 to 400 °C is related to the decarbonation of organic matters and LDH structure decomposition. Nearly 5.1% of weight loss was found from 500 to 660 °C, which was ascribed mostly to the dehydroxylation of the OH-groups of LDH. The last step at around 750 °C is attributed to the decomposition of sulfate as impurity, release of SO_3 and formation of the respective oxides in the spinel structure. The total mass losses of the samples throughout to 800 °C are approximately 4.3 wt%, 40.6 wt%, 34.8 wt%, 47.1 wt% and 40.1 wt% for Fe_3O_4, Zn,Al-LDH/Cit, Fe_3O_4/Zn,Al-LDH/Cit, Zn,Al-LDH/EDTA and Fe_3O_4/Zn,Al-LDH/EDTA, respectively. The comparison this data prove that magnetic composites have higher thermal stability than starting materials.

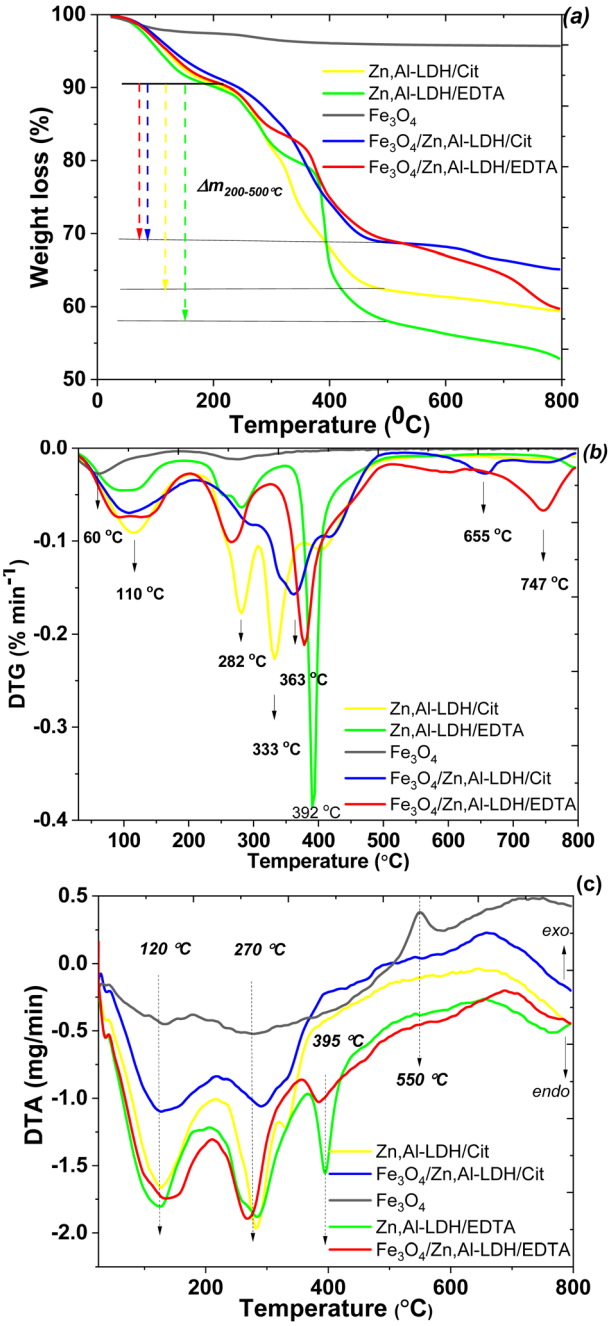

Fig. 7 TG (a), DTG (b) and DTA (c) curves of the prepared samples.

To determine the overall loading of the intercalated organic phase of the samples were used the value of weight loss at temperature range from 200 to 500 °C (Fig. 7a). According to the TG curves the amount of organic groups is about 0.040 mmol g^{-1} for Zn,Al-LDH/Cit, 0.028 mmol g^{-1} for Fe_3O_4/Zn,Al-LDH/Cit, 0.029 mmol g^{-1} for Zn,Al-LDH/EDTA and 0.015 mmol g^{-1} for Fe_3O_4/Zn,Al-LDH/EDTA. It can be seen that the amount of organic groups en Fe_3O_4/Zn,Al-LDH/Cit sample is higher than en Fe_3O_4/Zn,Al-LDH/EDTA.

It was ascertained from the EDX spectra (Fig. S4†) the presence of Al and Zn elements peaks with the other major peaks like C, O, N. The molar ratios of Zn/Al in the samples were observed to be 2.0–2.1. Using the atomic absorption spectrometry and total organic carbon analysis data, the chemical composition of intercalated compounds were determined. Atomic absorption spectroscopy gives weight percent on the order of 56% for Zn and 27% for Al. This result confirms the content of Zn : Al with a molar ratio of 2 : 1, which is in good agreement with the EDX data and ratio used in the synthesis. TGA measurements reveal water loss of about 10% up to 150 °C (Fig. 7a). A chemical composition of $[Zn_4Al_2(OH)_{12}](H_2EDTA)\cdot 8H_2O$ and $[Zn_4Al_2(OH)_{12}]Cit\cdot 8H_2O$ are typical for obtained samples. The Fe_3O_4 content in the magnetic nanocomposite was 18.79 wt%. Similarly, the chemical composition for the obtained magnetic adsorbents were determined such as $Fe_3O_4[Zn_4Al_2(OH)_{12}]Cit\cdot 8H_2O$ and $Fe_3O_4[Zn_4Al_2(OH)_{12}](H_2EDTA)\cdot 8H_2O$.

3.2. Uranium(VI) adsorption onto obtained samples

The efficiency of magnetic nanocomposites and corresponding starting materials as adsorbents to remove U(VI) from water medium was evaluated by the impact of pH, contact time, porosity features and coexisted ions. The advantages and limitations several of obtained adsorbents discovered.

3.2.1 Effect of pH and carbonate ions. The pH value plays one of the most important role in the adsorption processes. Obviously, the variation of pH could be affect to the surface chemistry of the obtained materials and the types and distribution of U(VI) species in the solution. The effectiveness U(VI) removal by obtained samples at different pH was shown in Fig. 8 and S2.†

The increase of U(VI) adsorption on Zn,Al-LDH/Cit and Fe_3O_4/Zn,Al-LDH/Cit was observed at 4.5 < pH < 8.0 (Fig. 8). The maximum U(VI) uptake on Fe_3O_4/Zn,Al-LDH/Cit was demonstrated at pH 7.0. The high-level adsorption at pH 7.0–8.0 kept on Zn,Al-LDH/Cit sample, then whereas U(VI) uptake was significantly decreased at pH > 8.0. However, the removal percentage of U(VI) on Zn,Al-LDH/Cit and Fe_3O_4/Zn,Al-LDH/Cit samples was no more than 60%. Quantitative removal of U(VI) at 6.0 ≤ pH ≤ 8.0 was achieved for Fe_3O_4, Zn,Al-LDH/EDTA and Fe_3O_4/Zn,Al-LDH/EDTA samples. For Zn,Al-LDH/EDTA and Fe_3O_4/Zn,Al-LDH/EDTA samples, the significant increase of U(VI) uptake was observed at pH 4.0–6.0, and then remained at pH 6.0–8.0. The slight decrease of U(VI) adsorption was found at pH > 8.5. Similar pH removal range was observed for Fe_3O_4, Zn,Al-LDH/EDTA and Fe_3O_4/Zn,Al-LDH/EDTA samples. These data demonstrated likeness of the samples surface properties. Besides, the EDTA intercalated samples and magnetite shows the highest adsorption performance toward U(VI) than for citrate-containing specimens. The reason for this phenomenon might be the interaction with functional groups with some hydroxides as agree with XRD or internal molecular interaction of adsorbents under various pH. Thus, the part of the surface groups (such as M–OH) probably were blocked by functional citric groups of Zn,Al-LDH/Cit and Fe_3O_4/Zn,Al-LDH/Cit, resulting in lower adsorption efficiency. Nevertheless, for all studied adsorbents the maximum removal of U(VI) was achieved from solution at pH range from 6.0 to 8.0.

In general, U(VI) ions forming of UO_2^{2+}, $(UO_2)_2(OH)_2^{2+}$, UO_2OOH^+, $(UO_2)_3(OH)_5^+$, $(UO_2)_4(OH)_7^-$, $UO_2(CO_3)_2^{2-}$ and $UO_2(CO_3)_3^{4-}$ species in aqueous solution upon contact with the air (Fig. S3†).[6] The prevail UO_2^{2+} species in the acidic range (pH < 5) is observed. The pH in the environmental water is mainly 7.5–8.3, where the typically carbonate/bicarbonate is ubiquitous and often present relatively high concentration (near 5×10^{-3} mol L^{-1}) both natural and wastewaters. Predominant species of U(VI) in carbonate-containing waters are $UO_2(CO_3)_3^{4-}$ (80–90%), while also including smaller amounts of $UO_2(CO_3)_2^{2-}$ and insignificant concentrations of uranyl hydroxide complexes. (*e.g.*, ground water, uranium tailings wastewater).

It known, the adsorbent surface charges are influence the intensity and nature of interactions between the adsorption sites and U(VI) ions. The critical parameter of these features is the pH_{pzc} value.[44,49] The determination of pH_{pzc} of obtained adsorbents was performed at $pH_{initial}$ from 2.0 to 10.0 and the experimental data are presented in Fig. 9. The results of pH_{final} have been reformatted as ΔpH ($pH_{final} - pH_{initial}$, dot lines in the Fig. 9) *versus* $pH_{initial}$. Here the advantage of operating at similar adsorbents is obvious, because of virtually straight line of high slope extends well beyond of the x intercept.

With the available experimental data, the pH_{pzc} of Zn,Al-LDH/Cit, Zn,Al-LDH/EDTA, Fe_3O_4/Zn,Al-LDH/EDTA and Fe_3O_4/Zn,Al-LDH/Cit samples was determined as 8.53, 6.93, 7.34 and 6.91, respectively (Fig. 8). In this line, compared to Zn,Al-LDH/Cit and Fe_3O_4/Zn,Al-LDH/Cit samples the pH_{pzc} of Zn,Al-LDH/EDTA and Fe_3O_4/Zn,Al-LDH/EDTA composites were observed in the lower pH range (Fig. 9). The difference in pH_{pzc} values can be explained by the presence of available various acidic functional groups in the samples. At this state, the surface of samples were positive charged at pH < pH_{pzc}. Therefore in this range pH, the charged magnetic composites and initial samples would attracted to cation-exchange and complexation reaction with cationic forms of U(VI), thus resulted in the great increased pH of suspensions (Fig. S4†). During the process of U(VI) removal at pH > pH_{pzc} using obtained samples the $pH_{initial}$ was decreased to pH_{final} could be ascribed the anion-exchange between negative charged of adsorbents and the dominated at this pH negative charged of carbonate U(VI) complexes species.

The high-level uptake of U(VI) on magnetic composites and initial samples at pH 6.0–8.0 could be explain by complexation reaction of U(VI) with the Zn,Al-LDH/Cit, Zn,Al-LDH/EDTA, Fe_3O_4/Zn,Al-LDH/EDTA and Fe_3O_4/Zn,Al-LDH/Cit samples. The magnetic composite based on Zn,Al-LDH with interlayer EDTA ions is more effective in this range of pH, in contrast to

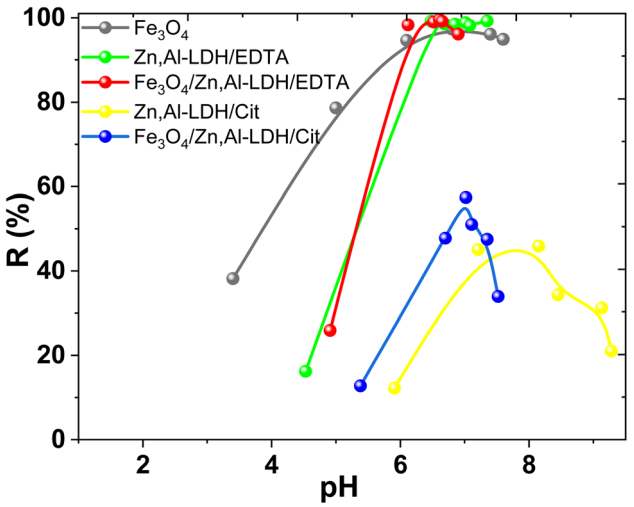

Fig. 8 Effect of pH on U(VI) removal by obtained samples (conditions: C_0(U(VI)) = 0.1 mmol L^{-1}, V/m = 500 cm^3 g^{-1}, time 1 h).

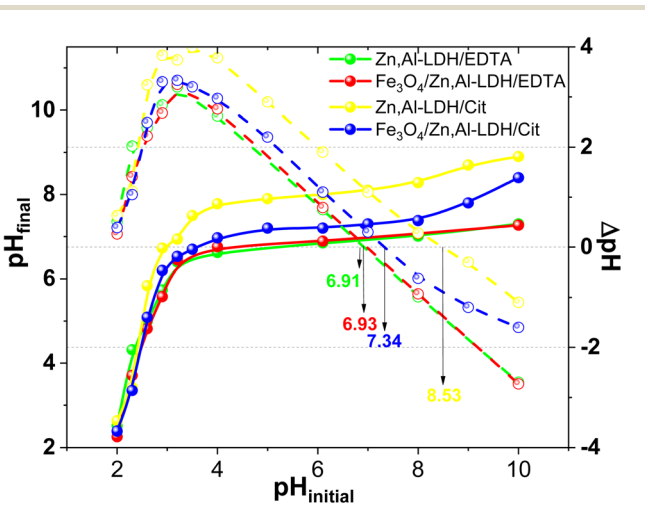

Fig. 9 The determination of pH_{pzc} of obtained adsorbents (conditions: m = 0.025 g, V = 50 mL, time 24 h, $C(NaClO_4)$ = 0.1 M).

Zn,Al-LDH/Cit and Fe_3O_4/Zn,Al-LDH/Cit samples. This fact confirms the predominant role of the chelating ligands in the interlayer space of LDH-based materials and indicates a higher binding strength of U(VI) specifically with EDTA groups of the Fe_3O_4/Zn,Al-LDH/EDTA. These results suggest that EDTA groups were intercalated into the interlayer space of the Fe_3O_4/Zn,Al-LDH/EDTA, which was attributed to its high specific surface area, and were beneficial for the removal of U(VI) ions. In addition, it is very likely that U(VI) is bound by additional active sorption centers of magnetite (Fe–OH groups) too.

3.2.2 Effect of contact time. The effect of contact time on adsorption of U(VI) onto Fe_3O_4/Zn,Al-LDH/EDTA and Fe_3O_4/Zn,Al-LDH/Cit samples at 25 °C was illustrated (Fig. 10).

The U(VI) uptake on the Fe_3O_4/Zn,Al-LDH/EDTA material increased dramatically in the first 5 min. While on the Fe_3O_4/Zn,Al-LDH/Cit the recovery of U(VI) increased slowly and attained plateau finally. In this case, the adsorption of U(VI) achieved equilibrium within more than 1 hour and the removal percentages does not exceed ~30%. The slower kinetics of Fe_3O_4/Zn,Al-LDH/Cit is could be attributed to the intraparticle diffusion of uranium(VI) into the inner pores of adsorbent or the ion exchange in the interface layer of LDH. The fast adsorption on Fe_3O_4/Zn,Al-LDH/EDTA should be attributed to the features

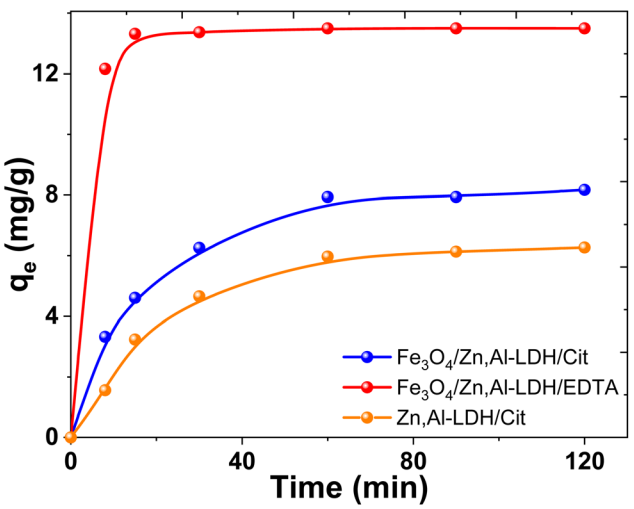

Fig. 10 Effect of contact time on U(VI) adsorption on several obtained adsorbents (conditions: C_0(U(VI)) = 0.1 mmol L^{-1}, pH_0 7.5, V/m = 500 mL g^{-1}).

porous layered structure with high permeability, probably because the EDTA motifs in the interlayer space of the LDH facilitate the acceleration of the diffusion of U(VI) ions both within the pores as well as at the surface.

Lagergren method pseudo-first-order and pseudo-second-order kinetic models[50,51] were applied to analyze the adsorption rate based on kinetic data (Fig. 10).[52] The relative parameters calculated from the two models were listed in Table 2.

It evidently manifest (Fig. S4†) that the experimental and calculated q_e values fitted pretty well by the pseudo second-order model remaining nearly constant with the perfect linearity R^2 (over 0.9841), demonstrating that the pseudo-second-order model can perfectly describe the uptake kinetics of U(VI) on the synthesized magnetic adsorbents. This effect further implies that the dominant mechanism for uranium(VI) removal on sample is chemisorption or strong complexation rather than mass transport.

3.2.3 Adsorption isotherms. To characterize the interaction of U(VI) ions with the obtained adsorbents the adsorption isotherms were studied at pH 7.5 (Fig. 11).

Fig. 11 exhibited that the adsorption capacities for U(VI) adsorption improved remarkably with the increase of U(VI) concentrations. This result indicated that higher U(VI) concentrations can provide higher capacity to U(VI) transportation *via* solution to the adsorbents interfacial layer, and thereby lead to more interaction between U(VI) and active sites. According to Giles classification,[53] obtained experimental isotherms adsorption of U(VI) can be described by various types of isotherms. Isotherm adsorption of UO_2^{2+} by Fe_3O_4/Zn,Al-LDH/EDTA can be considered as H-type, even though in this case a high slope was observed indicative of strong adsorbate–adsorptive interactions such as inner-sphere complexes. An Zn,Al-LDH/EDTA isotherm the slope initially increases with adsorptive concentration, but eventually stabilizes and becomes over increases as vacant adsorbent sites are filled. This type of isotherm indicates that at low concentrations the surface has a high affinity for the adsorptive, which significantly increases at higher concentrations. The adsorption isotherms of U(VI) on the other studied adsorbents may be assigned to L-type isotherms.[53] The L-shaped (or Langmuir type) isotherm is characterized by a decreasing slope as concentration increases since vacant adsorption sites decrease as the adsorbent becomes covered. Such adsorption behavior could be explained by the high affinity of the adsorbent for the adsorptive at low concentrations, which then decreases as concentration increases. It can be seen that the

Table 2 Experimental adsorption capacity and calculated kinetic parameters for adsorption U(VI) ions on obtained samples[a]

		Pseudo first-order model			Pseudo second-order model		
Samples	q_{exp} (mg g^{-1})	q_e (mg g^{-1})	K_1 (min^{-1})	R^2	q_e (mg g^{-1})	K_2 (g (mg min)$^{-1}$)	R^2
Zn,Al-LDH/Cit	7.65	5.74	0.014	0.8716	6.85	0.013	0.9841
Fe_3O_4/Zn,Al-LDH/Cit	9.18	6.12	0.018	0.8687	8.61	0.016	0.9915
Fe_3O_4/Zn,Al-LDH/EDTA	14.55	2.61	0.011	0.2592	12.92	0.600	1.0000

[a] q_t and q_e – adsorption capacity at time t and equilibrium conditions, respectively; K_1 and K_2 are the rate constants pseudo first-order and pseudo second-order models, respectively.

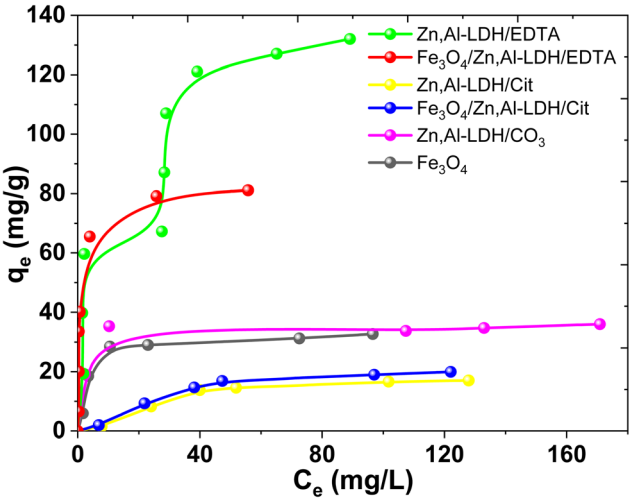

Fig. 11 Isotherms adsorption of U(VI) by magnetic nanocomposites and starting materials (conditions: $C_{U(VI)} = 0.15–0.90$ mmol L^{-1}, pH 7.5, $V/m = 500$ mL g^{-1}, contact time 1 h).

adsorption ability of Fe_3O_4/Zn,Al-LDH/EDTA sample for U(VI) ions is higher than Fe_3O_4/Zn,Al-LDH/Cit. The adsorption capacity of pristine Fe_3O_4 nanoparticles should come from its porous microstructures, but its small surface area lead to its lower adsorption performance. The Zn,Al-LDH/CO_3 show a better adsorption ability than pristine magnetite.

According to the isotherm data the adsorption capacities is about 0.12 mmol g^{-1} (32.73 mg g^{-1}) for Fe_3O_4, 0.13 mmol g^{-1} (36.05 mg g^{-1}) for Zn,Al-LDH/CO_3, 0.06 mmol g^{-1} (17.03 mg g^{-1}) for Zn,Al-LDH/Cit, 0.45 mmol g^{-1} (131.22 mg g^{-1}) for Zn,Al-LDH/EDTA, 0.07 mmol g^{-1} (19.95 mg g^{-1}) for Fe_3O_4/Zn,Al-LDH/Cit and 0.29 mmol g^{-1} (81.12 mg g^{-1}) for Fe_3O_4/Zn,Al-LDH/EDTA. The adsorption capacity for U(VI) on all obtained materials decreased in the following order: Zn,Al-LDH/EDTA > Fe_3O_4/Zn,Al-LDH/EDTA > Zn,Al-LDH/CO_3 ~ Fe_3O_4 > Fe_3O_4/Zn,Al-LDH/Cit > Zn,Al-LDH/Cit. This one is matches pretty well to the stability of the corresponding chelate U(VI) compounds in solution: the stability constants of U(VI) with citrate and EDTA groups are log β(Cit) = 8.75 and log β(EDTA) = 19.7, respectively (Table S1†).[54]

The adsorption data are usually interpreted using several adsorption equilibrium models such as the Langmuir and Freundlich.[55,56] The Langmuir model is the most popular model to describe the adsorption properties of LDH based adsorbents.[27] The fitting curves and calculation parameters of Langmuir and Freundlich models for the U(VI) adsorbed in the obtained adsorbents according to linear transformation of the isotherm data were presented in Fig. S6† and Table 3.

By comparing the average values of R^2 fitted by the Langmuir and Freundlich models, it can be found that the adsorption of U(VI) on obtained samples are mostly correlated with Langmuir isotherm than that for Freundlich model. The chemical nature of the sorption is actually in good agreement with mono-layered and uniform sorption indicated by Langmuir model, as well as our expectation that U(VI) ions are adsorbed through complexation with the EDTA-groups on the surface of adsorbents. For Zn,Al-LDH/Cit and Fe_3O_4/Zn,Al-LDH/Cit samples, the Freundlich model show better fitting with adsorption data.

The comparison of adsorption parameters of the adsorbents synthesized in this work with other published adsorbents for the removal U(VI) ions using magnetite-based adsorbents are summarized and tabulated in Table 4.

Obviously, the Fe_3O_4/Zn,Al-LDH/EDTA slightly lower adsorption capacity than the several previously reported adsorbents (Table 4). Most importantly, this adsorption technique with Fe_3O_4/Zn,Al-LDH/EDTA nanoadsorbent would enable simple magnetic separation and available instrumentation combine with the low sample and reagents consumption as well as pH values corresponding to uranium(VI)-polluted wastewater.

3.2.4 Coexisting metal ions interference. In the practical tasks, effect of macro/microcomponents of environmental water such as anions (HCO_3^-/CO_3^{2-}) and cations (Ca^{2+}, Na^+, K^+, *etc.*) onto obtained adsorbents performance was tested from model solution. The water samples were spiked with approximately 20–200 mg L^{-1}. The concentration of target U(VI) ions before testing was 0.1 mmol L^{-1}. Also, the dissolved organic matter (DOM) also has a significant effect, due to their mobile and actively cycling organic matter fraction, influences to the removal processes anionic complexes of U(VI) in the aquatic environments. The influence of DOM was studied using fulvic acids as model organic compounds (Fig. 12).

Table 3 Fitting parameters obtained from the linear transformation of the isotherm data for various samples

		Langmuir isotherm model $\frac{C_e}{q_e} = \frac{C_e}{q_m} + \frac{1}{K_L q_m}$			Freundlich isotherm model $\log q_e = \log K_F + \frac{1}{n} \log C_e$		
Adsorbent	q_{exp}, (mg g^{-1})	q_m, (mg g^{-1})	K_L, (L μg^{-1})	R^2	K_F, (mg$^{1-1/n}$ $L^{1/n}$ g^{-1})	$1/n$	R^2
Fe_3O_4	32.73	33.98	0.23	0.9970	8.65	0.3357	0.6890
Zn,Al-LDH/CO_3	36.05	35.71	0.48	0.9984	20.57	0.4857	0.6323
Zn,Al-LDH/Cit	17.02	28.65	0.01	0.754	0.48	0.8076	0.8755
Zn,Al-LDH/EDTA	130.04	142.86	0.09	0.9217	28.77	0.3464	0.7629
Fe_3O_4/Zn,Al-LDH/Cit	19.95	33.56	0.01	0.7622	0.61	0.7903	0.8704
Fe_3O_4/Zn,Al-LDH/EDTA	81.12	112.36	0.11	0.8105	12.62	0.634	0.7958

Table 4 The removal performance of magnetite-based adsorbents for removal U(VI) ions from various water samples at pH ≥ 6[a]

Adsorbent	Preparation and modification of adsorbents	pH	Adsorption conditions	Adsorption mechanism and isotherm model	Ref.
Fe_3O_4/Mg,Al-LDH/citrate	Co-precipitation; Mg–Al-LDH, citrate	6	q_e 180 mg g^{-1}, 4 h, 25 °C	Formation of chelate complex; Freundlich model	39
Sal-APS-FMNPS	Co-precipitation; salicylaldehyde	7	q_e 49 mg g^{-1}	—	57
Fe_3O_4	Co-precipitation; ammonium and phosphate	9	q_e 70.7 mg g^{-1}, 2 h	Electrostatic and chelating attraction	58
MnO_2–Fe_3O_4–rGO	Hydrothermal, decorated graphene oxide	6	q_e 95.24 mg g^{-1}, 3 h	Surface complexation, electrostatic attraction and cation exchange	59
Ketoxime-Fe_3O_4@C	Solvothermal; carbon and ketoxime	6	q_e 38.7 mg g^{-1}, 2 h		60
HCC-Fe_3O_4	Hydrothermal; chitosan	7	q_e 263.7 mg g^{-1}, 3 h	Interaction with OH and NH_2-groups	61
Fe_3O_4/C/Ni–Al-LDH	Co-precipitation; carbon, Ni–Al-LDH	6	q_e 174 mg g^{-1}, 3 h	Surface adsorption and intercalation; Langmuir model	62
Magnetic oxine	Solvothermal; oxine (8-hydroxyquinoline)	7	q_e 125 mg g^{-1}, >4 h	Inner-sphere complexation	63 and 64
Fe_3O_4@SiO_2-AO	Hydrothermal; amidoxime	5	q_e 105.5 mg g^{-1} T^{-1} 298 K	—	65
Fe_3O_4@APTMS	Hydrothermal; aminopropyl groups	6	q_e 151.8 mg g^{-1}	Complexation with NH_2-groups	66
Fe_3O_4/Ca,Al-LDH (CMLH)	Co-precipitation; Ca-Al-LDH, hydroxyapatite	6	q_e 208 mg g^{-1}, 1 h	Surface adsorption and complexation	67
GO@LDH	One-pot hydrothermal; Ni,Al-LDH and GO	7–9	q_e 159, 7 mg g^{-1}	Surface complexation and electrostatic attraction	68
Zn,Al-LDH/EDTA, Fe_3O_4/Zn,Al-LDH/EDTA	Co-precipitation; Zn,Al-LDH, EDTA	7.5	q_e 131.22 mg g^{-1}, 5 min, 25 °C, q_e 81.12 mg g^{-1}, 5 min, 25 °C	Ion-exchange and complexation; Langmuir model	This work

[a] Sal-APS-FMNPS – magnetic nanoparticles with salicylaldehyde groups; rGO – reduced graphite oxide; CMLH – calcined magnetic Ca,Al layered double hydroxide/hydroxyapatite; HCC-Fe_3O_4 – magnetic hydrothermal cross-linking chitosan; Fe_3O_4@BP – bisphosphonate-modified magnetite nanoparticles.

From Fig. 12, as the concentration of co-existing ion increased from 20 mg L^{-1} to 200 mg L^{-1}, the effect of CO_3^{2-}/HCO_3^-, FA, Na^+ and Ca^{2+} ions on U(VI) adsorption was comparatively weak for Fe_3O_4/Zn,Al-LDH/EDTA, whereas the effect of these ions at using Zn,Al-LDH/Cit and Fe_3O_4/Zn,Al-LDH/Cit was strong in the wide range of their concentrations (up to 200 mg L^{-1}). This result indicates that Fe_3O_4/Zn,Al-LDH/EDTA exhibits the high selectivity and its application would be expected to be feasible in most cases of environmental water treatments (with high concentration of CO_3^{2-}/HCO_3^-).

The components typical of environmental and wastewaters aren't reduce the efficiency of removal of U(VI) from large volumes of humus-containing aqueous solution by the Fe_3O_4/Zn,Al-LDH/EDTA. Since, the stability constants of complexes of multiply charged U(VI) ions with EDTA groups are found the largest among one or two valence metal ions, which is the main reason for selectivity of Fe_3O_4/Zn,Al-LDH/EDTA towards U(VI) (Table S1†).[41] Such phenomenon illustrated that the main mechanism for the uptake of radionuclide is complexation with the ligand of the inner surface of LDH space. So, Fe_3O_4/Zn,Al-LDH/EDTA could employed to efficiently remove U(VI) ions from multicomponent solution.

3.3. Effect of various factors on removal efficiency and adsorption mechanism

Characterization of both nanocomposites (as-prepared and metal-adsorbed) was done using FTIR spectra to identify the functional groups interaction of adsorbed metal ions with organic species on the adsorbents (Fig. 13).

The new band at ~1520 cm^{-1} in the metal-loaded sample (Fig. 13) is assigned to the antisymmetric vibration of C–O–[O=U=O]$^+$. This peak has a significant red-shift compared to the corresponding peak of aqueous UO_2^{2+} (~963 cm^{-1}), indicating the chemical bonding of UO_2^{2+} with the intercalated EDTA-groups.

Based on the above mentioned results, there are possible three main mechanisms for the removal of U(VI) forms (Fig. S3†) on magnetic nanocomposites (Scheme 2), which can be expressed as follows:

(1) Surface complexation. It is a kind of complexation by intercalated groups in the inner- and outer-layers of magnetic composites with U(VI) ions (as evidenced by FTIR), which is mainly based on abundant hydroxyl groups of layered structure and intercalated chelating groups:

$$Fe_3O_4/Zn,Al\text{-}LDH/H_2EDTA + UO_2^{2+} \rightarrow Fe_3O_4/Zn,Al\text{-}LDH/EDTA/UO_2 + 2H^+$$

or

$$Fe_3O_4/Zn,Al\text{-}LDH/H_2EDTA + (UO_2)_3(OH)_5^+ \rightarrow Fe_3O_4/Zn,Al\text{-}LDH/HEDTA/(UO_2)_3(OH)_5 + H^+$$

$$M\text{–}O\text{–}H + UO_2^{2+} \rightarrow M\text{–}O\cdots UO_2^{2+} + H^+$$

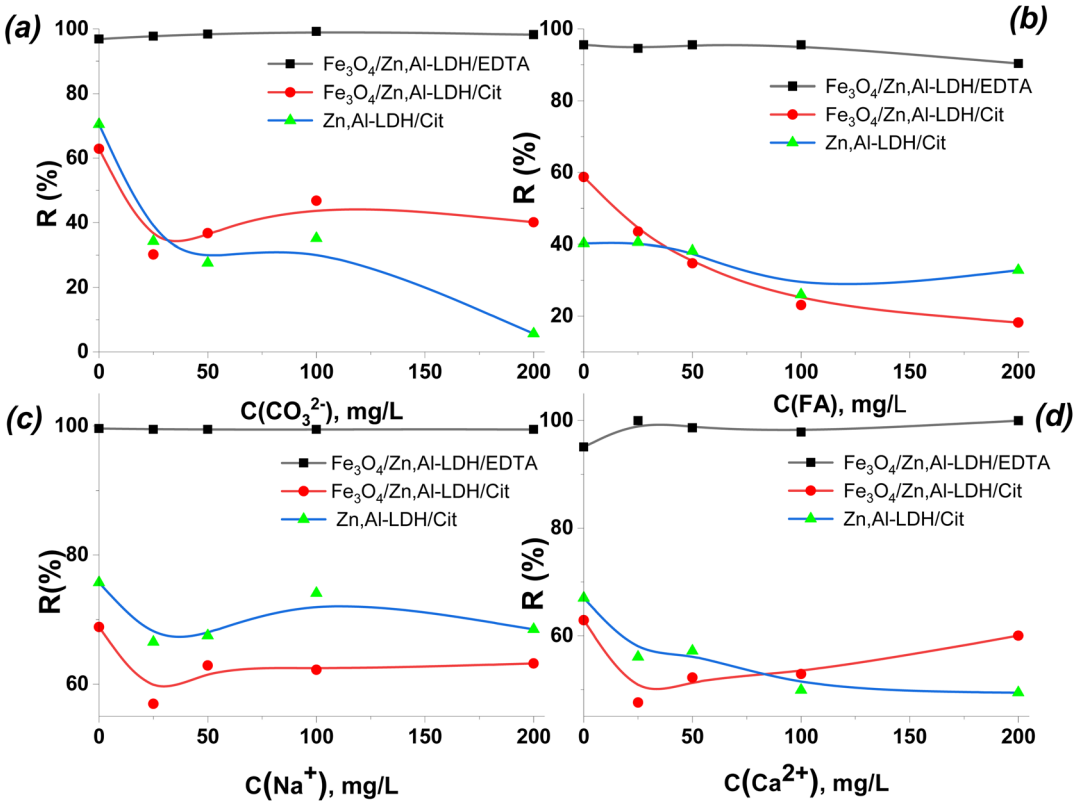

Fig. 12 Effect of the concentration of CO_3^{2-}/HCO_3^- (a), FA (b), Na^+ (c) and Ca^{2+} (d) ions on the sorption of U(VI) by the synthesized adsorbents (conditions: C(U(VI)) = 0.1 mmol L^{-1}, pH_0 6.0, V/m = 500 cm^3 g^{-1}).

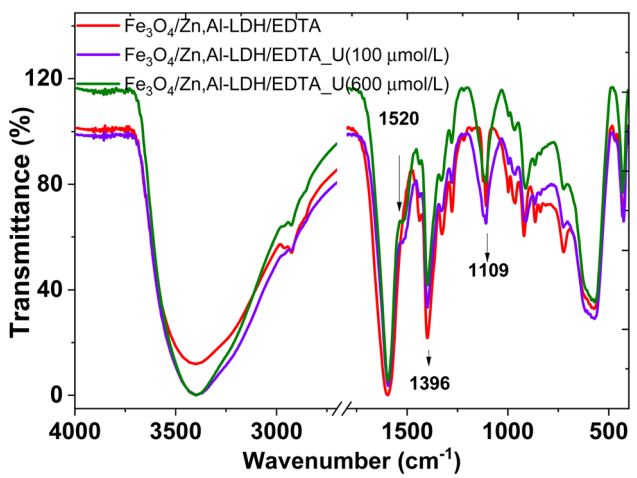

Fig. 13 FTIR spectra of initial (Fe_3O_4/Zn,Al-LDH/EDTA) and resulting samples after adsorption U(VI) from solutions with various concentration.

$$M\text{–}O\text{–}H + UO_2^{2+} \rightarrow M\text{–}O\text{–}H\cdots UO_2^{2+}$$

M = Zn(II), Al(III) and Fe(III)

Surface adsorption involves the bonding of U(VI) ion species to the hydroxyl units on the external surface of the LDH. So, interaction of the U(VI) ions species involves a network of hydrogen bonds between the metal ions species and the hydroxyl layers. By the synergism of the intercalation groups and the surface adsorption, a mass of U(VI) will be attracted to the surfaces of LDH and then adsorbed, leading to the high adsorption capacity. In the metal-adsorbed sample, the UO_2^{2+} binding with EDTA-groups – forms neutral salts inside the gallery of LDH-support.

(2) Ion-exchange. The Zn(II), Al(III) and Fe(III) surface sites on magnetic composites can react with U(VI) ions *via* ion exchange:

$$M\text{–}O\text{–}H + UO_2^{2+} \rightarrow M\text{–}O\text{–}UO_2^{+} + H^+$$

$$M\text{–}O\text{–}H + UO_2(CO_3)_2^{2-} \rightarrow M\text{–}UO_2(CO_3)_2^{-} + OH^-$$

$$Fe_3O_4/Zn,Al\text{-}LDH/H_2EDTA + UO_2(CO_3)_2^{2-} \rightarrow Fe_3O_4/Zn,Al\text{-}LDH/UO_2(CO_3)_2 + H_2EDTA^{2-}$$

Since the interlayer anions are easily exchangeable, the anions in the interlayer can be exchanged by anions, *i.e.* so that it makes LDH useful for removal hazardous anionic forms of U(VI) from aqueous solution.

(3) Redox-precipitation. In this type of mechanism, a dissolution of the Fe_3O_4 loaded on LDH occurs, supplying the sorption system with EDTA groups which have high affinity for U(VI) ions, precipitating and forming thus a new phase UO_2, which can be expressed as eqn:

$$2Fe^{2+} + UO_2^{2+} \rightarrow 2Fe^{3+} + UO_2$$

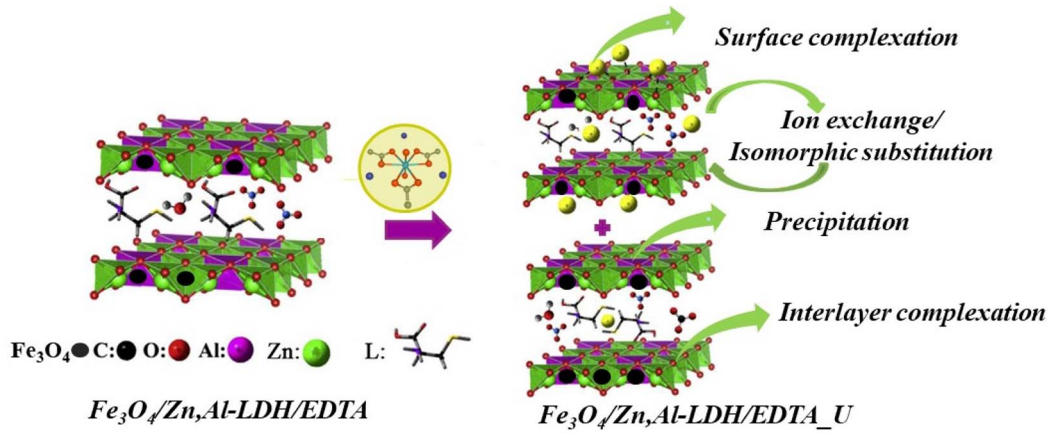

Scheme 2 The schematic diagram of the main adsorption mechanisms for U(VI) ions removal using Fe_3O_4/Zn,Al-LDH/H_2EDTA sample.

Table 5 Effect of the adsorbent dose on the efficiency of U(VI) removal from environmental and wastewaters

Adsorbent	Adsorbent dose, g L^{-1}	Recovery, %	
		Environmental water	Wastewater
Fe_3O_4/Zn,Al-LDH/EDTA	1	99.4	95.8
	6	99.8	99.5
Fe_3O_4/Zn,Al-LDH/Cit	1	28.8	10.3
	6	40.9	22.7

Therefore, U(VI) adsorption on the samples was mainly corelated to the ion-exchange and surface complexation due to the OH-groups from LDH, and complexation reaction with EDTA-ligands as well as redox reactions of iron(II) ions from magnetite, which indicated that the effective adsorption of Fe_3O_4/Zn,Al-LDH/EDTA was resulting to the synergetic effect all components of nanocomposite. Further studies are needed to more precisely characterize the detailed adsorption mechanism.

3.4. Analytical performance for real water samples

The effectiveness of the obtained magnetic nanocomposites was studied to water purification in real systems. The environmental and wastewater samples were analyzed using various adsorbent doses as influential parameters that directly affect the removal of pollutants from aqueous solution and cost effectiveness of obtained adsorbents for practical applications (Table 5). The effect of the adsorbent dose on the removal of U(VI) from water samples were studied during of 1 hour.

The adsorption percentage of U(VI) at adsorbents dose of 1 g L^{-1} is 99.4% and 28.8% for Fe_3O_4/Zn,Al-LDH/EDTA and Fe_3O_4/Zn,Al-LDH/Cit, respectively. Theoretically,[25] the increase in adsorbent dosage results in enhanced percentage removal efficiency, *i.e.* this may be due to low adsorbent dosage, leading to the dispersal of magnetic nanocomposites into the aqueous solution. The increase in removal percentage of U(VI) from 95.8% to 99.5% into wastewater using Fe_3O_4/Zn,Al-LDH/EDTA are related to the increase in the from dose of 1 g L^{-1} to 6 g L^{-1}. In this case, adsorbent active sites were completely exposed, which eases the adsorption capability of U(VI). In this process, the adsorbent surface sites are saturated quickly, leading to high adsorption capacity. Generally, the Fe_3O_4/Zn,Al-LDH/Cit sample is low effective for purification water even at adsorbent dose of 6 g L^{-1}. Therefore, the optimum adsorbent dose is kept at 6 g L^{-1} for adsorption experiments.

Based on the high selectivity provided by using Fe_3O_4/Zn,Al-LDH/EDTA sample the recoveries of U(VI) in the 6 g L^{-1} ranged from 99.8% for environmental water, 99.5% for wastewater was satisfactory. Therefore, the studied sorption material with magnetic properties is highly efficient, highly selective and promising for the purification (post-purification) of aqueous media, including natural waters and waste water of uranium processing enterprises.

4. Conclusions

In this study, we prepared two magnetic nanocomposites based on magnetite and Zn,Al-layered double hydroxides intercalated with citric (or EDTA) groups and successfully applied their as effective adsorbent materials for the removal of U(VI) ions from various origin aqueous solution. The adsorption experiments were conducted by a batch technique, and the conditions have been optimized to be a pH value of 6.0–8.0, V/m 500 mL g^{-1} with high uptake time (5 min), which result was superior to the

previously reported adsorbents. The maximum adsorption capacity of the Fe_3O_4/Zn,Al-LDH/EDTA nanocomposite for the uranium(VI) ion was 81.2 mg g^{-1} at pH 8.0, and high specificity and selectivity for U(VI) when coexisting with cations (such as Na(I) and Ca(II)), anions (HCO_3^-/CO_3^{2-}) and dissolved organic motives. The adsorption followed pseudo-second-order kinetics and the equilibrium data of Fe_3O_4/Zn,Al-LDH/EDTA were well fitted with Langmuir isotherms. Also, the nanocomposite can be easily separated from the solution by an external magnetic field after the adsorption process. It provides a rapid and effective way for removing the nanoadsorbent from aqueous suspension after the adsorption process during environmental pollution clean-up treatment. Considering low-cost adsorbent synthesis environmental safety and high selectivity, as well as the possibility of complete automation of the technological process of extracting U(VI) from large volumes uranium-contaminated waters due to the use of magnetic separation, as well as reduce the cost of treatment and prevent secondary pollution of environmental objects. The obtained results illustrate that Fe_3O_4/Zn,Al-LDH/EDTA could be a perfect candidate as an adsorbent for the removal of U(VI) from wastewaters.

Conflicts of interest

The authors declare that they have no known competing financial interests or personal relationships that could have appeared to influence the work reported in this paper.

Acknowledgements

Dr Natalia Kobylinska acknowledges the financial support given by the University of Oviedo (Spain) from the Spanish Ministry of Science and Innovation (PID 2020-113558RB-C41). The authors grateful Armed Forces of Ukraine for the service and sacrifice.

References

1 E. Wilds, *Health Phys.*, 2013, **104**, 232–233.
2 V. Kashparov, B. Salbu, S. Levchuk, V. Protsak, I. Maloshtan, C. Simonucci, C. Courbet, H. L. Nguyen, N. Sanzharova and V. Zabrotsky, *J. Environ. Radioact.*, 2019, **208–209**, 106025.
3 L. S. Keith, O. M. Faroon and B. A. Fowler, *Handb. Toxicol. Met.*, 2007, 881–903.
4 M. O. Barnett, P. M. Jardine, S. C. Brooks and H. M. Selim, *Soil Sci. Soc. Am. J.*, 2000, **64**, 908–917.
5 R. W. Herschy, *Encycl. Earth Sci. Ser.*, 2012, 876–883.
6 D. Langmuir, *Geochim. Cosmochim. Acta*, 1978, **42**, 547–569.
7 J. Li and Y. Zhang, *Procedia Environ. Sci.*, 2012, **13**, 1609–1615.
8 J. Wang and S. Zhuang, *Rev. Environ. Sci. Bio/Technol.*, 2019, **18**, 437–452.
9 H. N. Bhatti and S. Hamid, *Int. J. Environ. Sci. Technol.*, 2014, **11**, 813–822.
10 A. Baeza, A. Salas and F. Legarda, *Sci. Total Environ.*, 2008, **406**, 24–34.
11 J. Shen and A. Schäfer, *Chemosphere*, 2014, **117**, 679–691.
12 M. Dulama, M. Iordache and N. Deneanu, *Inst. Nucl. Res.*, 2013, 80–87.
13 I. A. Katsoyiannis and A. I. Zouboulis, *Desalin. Water Treat.*, 2013, **51**, 2915–2925.
14 D. Rana, T. Matsuura, M. A. Kassim and A. F. Ismail, *Desalination*, 2013, **321**, 77–92.
15 Y. Hua, W. Wang, X. Huang, T. Gu, D. Ding, L. Ling and W. xian Zhang, *Chemosphere*, 2018, **201**, 603–611.
16 L. Newsome, K. Morris, D. Trivedi, N. Atherton and J. R. Lloyd, *Appl. Geochem.*, 2014, **51**, 55–64.
17 A. Liu, J. Liu, B. Pan and W. X. Zhang, *RSC Adv.*, 2014, **4**, 57377–57382.
18 H. Paar, A. S. Ruhl and M. Jekel, *Water Res.*, 2015, **68**, 731–739.
19 R. A. Crane, M. Dickinson, I. C. Popescu and T. B. Scott, *Water Res.*, 2011, **45**, 2931–2942.
20 M. A. Abu-Dalo, S. Nevostrueva and M. Hernandez, *Sci. Rep.*, 2020, **10**, 1–13.
21 N. Combernoux, L. Schrive, V. Labed, Y. Wyart, E. Carretier and P. Moulin, *Water Res.*, 2017, **123**, 311–320.
22 X. Yi, Z. Xu, Y. Liu, X. Guo, M. Ou and X. Xu, *RSC Adv.*, 2017, **7**, 6278–6287.
23 V. V. Kusumkar, M. Galamboš, E. Viglašová, M. Daňo and J. Šmelková, *Materials*, 2021, **14**, 1–29.
24 S. J. Coleman, P. R. Coronado, R. S. Maxwell and J. G. Reynolds, *Environ. Sci. Technol.*, 2003, **37**, 2286–2290.
25 M. Khorshidi, S. Asadpour, N. Sarmast and M. Dinari, *J. Mol. Liq.*, 2022, **348**, 118399.
26 W. Linghu, H. Yang, Y. Sun, G. Sheng and Y. Huang, *ACS Sustainable Chem. Eng.*, 2017, **1**, 1–31.
27 M. Zubair, M. Daud, G. McKay, F. Shehzad and M. A. Al-Harthi, *Appl. Clay Sci.*, 2017, **143**, 279–292.
28 M. Grafe, K. G. Bunney, S. Cumberland and G. Douglas, *ACS Omega*, 2017, **2**, 7112–7119.
29 S. Ma, L. Huang, L. Ma, Y. Shim, S. M. Islam, P. Wang, L. D. Zhao, S. Wang, G. Sun, X. Yang and M. G. Kanatzidis, *J. Am. Chem. Soc.*, 2015, **137**, 3670–3677.
30 Y. Cai, Y. Ma, J. Feng, M. Zhu, X. Wang, Z. Lv, M. Fang, X. Tan and X. Wang, *Chem. Eng. J.*, 2020, **402**, 125510.
31 X. Wang, Y. Cai, T. Han, M. Fang, K. Chen and X. Tan, *J. Hazard. Mater.*, 2020, **399**, 123081.
32 S. M. Husnain, W. Um, Woojin-Lee and Y. S. Chang, *RSC Adv.*, 2018, **8**, 2521–2540.
33 D. Das, M. K. Sureshkumar, S. Koley, N. Mithal and C. G. S. Pillai, *J. Radioanal. Nucl. Chem.*, 2010, **285**, 447–454.
34 M. J. O'Hara, J. C. Carter, C. L. Warner, M. G. Warner and R. S. Addleman, *RSC Adv.*, 2016, **6**, 105239–105251.
35 W. Li, L. D. Troyer, S. S. Lee, J. Wu, C. Kim, B. J. Lafferty, J. G. Catalano and J. D. Fortner, *ACS Appl. Mater. Interfaces*, 2017, **9**, 13163–13172.
36 E. Calì, J. Qi, O. Preedy, S. Chen, D. Boldrin, W. R. Branford, L. Vandeperre and M. P. Ryan, *J. Mater. Chem. A*, 2018, **6**, 3063–3073.
37 X. M. Song, L. C. Tan, H. Y. Ma, Y. Guo, L. Zhu, X. Q. Yi, J. Y. Gao, R. J. Yang and Q. Dong, *Dalton Trans.*, 2017, **46**, 3347–3352.

38 L. N. Puzyrnaya, G. N. Pshinko, B. Yatsik, V. Y. Zub and A. A. Kosorukov, *Radiochemistry*, 2020, **62**, 50–61.
39 X. Zhang, L. Ji, J. Wang, R. Li, Q. Liu, M. Zhang and L. Liu, *Colloids Surf., A*, 2012, **414**, 220–227.
40 N. G. Kobylinskaya, E. A. Khainakova, M. E. Diaz-Garcia and V. N. Zaitsev, *Prot. Met. Phys. Chem. Surf.*, 2017, **53**, 675–684.
41 S. Su, Q. Liu, J. Liu, H. Zhang, R. Li, X. Jing and J. Wang, *Sci. Rep.*, 2017, **7**, 1–9.
42 L. A. Kaplan, *Limnol. Oceanogr.*, 1992, **37**, 1119–1125.
43 P. I. Ravikovitch, S. C. O'Domhnaill, A. V. Neimark, F. Schiith and K. K. Unger, *Langmuir*, 1995, **11**, 4765–4772.
44 J. Park and J. R. Regalbuto, *J. Colloid Interface Sci.*, 1995, **175**, 239–252.
45 A. L. Patterson, *Phys. Rev.*, 1939, **56**, 978–982.
46 W. H. Bragg and W. L. Bragg, *Proc. R. Soc. London, Ser. A*, 1913, **88**, 428–438.
47 D. E. Bugaris and J. A. Ibers, *Dalton Trans.*, 2010, **39**, 5949–5964.
48 M. Thommes, K. Kaneko, A. V. Neimark, J. P. Olivier, F. Rodriguez-reinoso, J. Rouquerol and K. S. W. Sing, *Pure Appl. Chem.*, 2015, **87**, 1051–1069.
49 M. Kosmulski, *Adv. Colloid Interface Sci.*, 2016, **238**, 1–61.
50 S. Azizian, *J. Colloid Interface Sci.*, 2004, **276**, 47–52.
51 Y. S. Ho and G. McKay, *Process Biochem.*, 1999, **34**, 451–465.
52 W. Rudzinski and W. Plazinski, *Langmuir*, 2008, **24**, 6738–6744.
53 C. H. Giles, D. Smith and A. Huitson, *J. Colloid Interface Sci.*, 1974, **47**, 755–765.
54 W. Verweij and J. P. Simonin, *J. Solution Chem.*, 2020, **49**, 1319–1327.
55 I. Langmuir, *J. Am. Chem. Soc.*, 1918, **40**, 1361–1403.
56 H. Freundlich, *Z. Physiol. Chem.*, 1907, **57U**, 385–470.
57 A. Rezaei, H. Khani, M. Masteri-Farahani and M. K. Rofouei, *Anal. Methods*, 2012, **4**, 4107–4114.
58 X. T. Chen, L. F. He, R. Z. Liu, C. Zhang, B. Liu and Y. P. Tang, *RSC Adv.*, 2015, **5**, 56658–56665.
59 L. Tan, J. Wang, Q. Liu, Y. Sun, X. Jing, L. Liu, J. Liu and D. Song, *New J. Chem.*, 2015, **39**, 868–876.
60 Q. Liu, W. Li, W. Zhao, L. Tan, X. Jing, J. Liu, D. Song, H. Zhang, R. Li, L. Liu and J. Wang, *RSC Adv.*, 2016, **6**, 22179–22186.
61 S. Long Yu, Y. Dai, X. Hong Cao, Z. Bin Zhang, Y. Hai Liu, H. Jie Ma, S. Jin Xiao, Z. Jun Lai, H. Jun Chen, Z. Yang Zheng and Z. Gao Le, *J. Radioanal. Nucl. Chem.*, 2016, **310**, 651–660.
62 X. Zhang, J. Wang, R. Li, Q. Dai, R. Gao, Q. Liu and M. Zhang, *Ind. Eng. Chem. Res.*, 2013, **52**, 10152–10159.
63 L. Tan, J. Wang, Q. Liu, Y. Sun, H. Zhang, Y. Wang, X. Jing, J. Liu and D. Song, *Colloids Surf., A*, 2015, **466**, 85–91.
64 L. Tan, Y. Wang, Q. Liu, J. Wang, X. Jing, L. Liu, J. Liu and D. Song, *Chem. Eng. J.*, 2015, **259**, 752–760.
65 Y. Zhao, J. Li, L. Zhao, S. Zhang, Y. Huang, X. Wu and X. Wang, *Chem. Eng. J.*, 2014, **235**, 275–283.
66 X. Zhang, J. Wang, R. Li, Q. Dai and L. Liu, *New J. Chem.*, 2013, **37**, 3914–3919.
67 S. Li, H. Bai, J. Wang, X. Jing, Q. Liu, M. Zhang, R. Chen, L. Liu and C. Jiao, *Chem. Eng. J.*, 2012, **193–194**, 372–380.
68 S. Yu, J. Wang, S. Song, K. Sun, J. Li, X. Wang, Z. Chen and X. Wang, *Sci. China: Chem.*, 2017, **60**, 415–422.